Journal of Innovative Optical Health Sciences
Vol. 2, No. 4 (2009) 353–364

World Scientific
www.worldscientific.com

MULTISPECTRAL UNMIXING OF FLUORESCENCE MOLECULAR TOMOGRAPHY DATA

MARIA SIMANTIRAKI*, ROSY FAVICCHIO*,†, STELIOS PSYCHARAKIS*,
GIANNIS ZACHARAKIS*,‡ and JORGE RIPOLL*
*Institute of Electronic Structure and Laser
Foundation for Research and Technology, Hellas 71110
Heraklion, Crete, Greece
†Institute of Molecular Biology and Biotechnology
Foundation for Research and Technology, Hellas 71110
Heraklion, Crete, Greece
‡zahari@iesl.forth.gr

Even though multispectral imaging is considered very significant in biological imaging, it is only commonly used in microscopy in a 2D approach. Here, we present a Fluorescence Molecular Tomography system capable of recording simultaneously tomographic data at several spectral windows, enabling multispectral tomography. 3D reconstructed data from several spectral windows is used to construct a linear unmixing algorithm for multispectral deconvolution of overlapping fluorescence signals. The method is applied on tomographic 3D fluorescence concentration maps in tissue-mimicking phantoms, yielding absolute quantification of the concentration of each individual fluorophore. Results are compared to the case when unmixing is performed in the raw 2D data instead of the reconstructed 3D concentration map, showing greater accuracy when unmixing algorithms are applied in the reconstructed data. Both the reflection and transmission geometries are considered.

Keywords: Optical tomography; multispectral imaging; *in vivo* imaging; fluorescence quantification.

1. Introduction

Fluorescence Molecular Tomography (FMT) has become an important imaging method for studying gene activity and molecular function inside small animal models.[1–7] FMT resolves molecular signatures in deep tissues by combining diffuse optical imaging principles with the use of fluorescent probes or markers.[5,8–12] The sample that carries the fluorescence probe is exposed to light at different positions and the emitted light is captured by a detector, such as a CCD camera.[8,13–16] Accurate physical models such as the transport theory or appropriate approximations such as the diffusion theory are used to describe light transport inside turbid media taking into account the optical properties of different tissue types.[17–20] Furthermore, of great importance in biological and biomedical research is the ability of a system to image more than one target simultaneously. This will allow visualizing multiple fluorescence probes or proteins at the same time. However, the biggest limitation to this approach is the spectral emission and/or excitation overlap amongst the fluorescence probes which coexist simultaneously in the sample, requiring the

‡Corresponding author.

development and application of elaborate spectral unmixing algorithms.

Multispectral optical imaging is a relatively new approach in the optical tomography field which combines the advantages of two already established optical modalities, optical imaging, and optical spectroscopy.[21–24] The advent of a variety of fluorescent dyes, probes and proteins and their expanded use has further boosted the development of multicolor analysis approaches. In these approaches, the spectrum of a mixture of fluorophores can be expressed as a linear combination of the spectra of each fluorophore with different weighting factors that can be obtained from spectroscopic measurements of the individual fluorophores.[21,24,25]

Up to date, many studies have been made on multicolor imaging, but usually without implicating simultaneously optical tomographic imaging and spectroscopy.[22,24] In all approaches of multicolor analysis of different cell types or tissues in tomography, the isolation of the fluorescence signals is based on the use of different filters. However, this is not always accurate especially if the emission spectra of the imaged samples overlap, which is the most common case for *in-vivo* applications. The final detected signal will thus be the combination of the emission spectra of all fluorophores that are excitable within the spectral window considered; it follows that separation of the fluorophores based on simple filter detection is possible only if the corresponding spectra are well separated. In all other cases, an algorithmic approach needs to be developed and used for calculating the independent contributions for each of the fluorescent molecules. Previous approaches for multicolor analysis express the overlap of fluorescent dyes or proteins as a linear combination of the different component's spectra. The spectral profile of each fluorophore is then used to calculate the equivalent weighted contribution to the total imaged spectrum and as a result enables the separation of each of the fluorophore contributions. In such approaches, a system of equations can be exactly defined when the number of measurements is equal to the number of fluorophores and a unique solution can be calculated. The simplest configuration is the use of different sets of filters that capture a complete set of images, one wavelength at a time.[25] A more efficient way is to combine a color CCD camera with multiple-bandwidth filters that provide short measurement times and can be very useful for intraoperative applications where fast *in situ* imaging is of importance.[22] A common application of multicolor detection methods is in microscopy where the spectral imaging system is combined with an epifluorescence microscope and a post-processing algorithm that solves a linear $m \times n$ system where m is the number of fluorophores and n the number of measurements, usually being the same as the measurements. More recently, multicolor approaches have been also applied to tomographic imaging to improve depth resolution.[26] The use of tomography as the unique method for recovering 3D quantitative information of fluorophore concentration for *in-vivo* whole body imaging is well established. Hence, multicolor methodologies need to be combined and incorporated to tomographic systems and algorithms. Initial reports[27] of such combined techniques provide the starting point for the future development of a complete tomographic methodology that will enable true *in-vivo* multicolor whole body imaging. To date, however, quantification of overlapping fluorescent signals and hence multiple fluorophore concentrations has not been realized in tomographic data, mainly due to the fact that spectral unmixing has been applied on the raw 2D data and not on volumetric reconstructions. Such an approach suffers from the fact that when treating raw data, light propagation through highly heterogeneous media, such as biological tissues, has not been taken into account. This results in inaccurate quantification of fluorophore concentrations.

In this paper, we report a multiwavelength system and method for quantitative tomographic localization of multiple fluorophores. Our approach is based on the existing FMT system and a newly designed spectral algorithm that can perform unmixing in tomographic reconstructions as well as 2D untreated images. After describing the experimental setup, we present the spectral unmixing algorithm introduced in our tomographic calculations which we then evaluate under varying conditions. We assess the quantification accuracy and tomographic quality of the unmixed data when the algorithm is applied to raw 2D data or to 3D tomographic data. The method is applied to an experimental study employing two fluorophores embedded in a tissue-like environment comprised of a liquid phantom measured in both reflection and transmission geometries in order to evaluate the algorithm. The results of the unmixed reconstructions are presented and the two approaches (unmixing raw 2D data and 3D tomographic data) as well as the two imaging geometries are compared. Finally, we

discuss our results and propose the best approach for *in-vivo* tomographic imaging as well as future steps to improve the effectiveness and accuracy of unmixing algorithms.

2. Materials and Methods

2.1. *FMT setup*

A schematic representation of the FMT setup is shown in Fig. 1. Illumination is provided by a cw Argon-Ion Laser (Laser Physics, Reliant 1,000 m, West Jordan, UT 84088 USA) (i). The laser emits at several wavelengths in the visible spectrum, the main lines being at 458, 488, and 514.5 nm. The laser light is directed to the imaging chamber and into the laser scanning device (Scancube 7, Scanlab, Germany) which incorporates a system of mirrors mounted on miniaturized galvanometer motors (ii). These mirrors are being controlled by in-house developed software and the laser beam can be controlled in the x–y plane of measurement, after being guided to the sample by using large rectangular mirrors (first surface mirrors, 4–6 Wave, 73 mm 116 mm, Edmund Optics). One mirror is mounted permanently on the ceiling of the box (iv), while the other one lies on the optical table and can be moved along a rail between two fixed positions altering the geometry of the experiment between reflection and transmission. For measurements in the reflection geometry the bottom mirror is moved forth so that the laser beam is directed to the top mirror and then to the sample from the side of the camera (iiia). For measurements in transmission geometry the bottom mirror is moved to the back position, so that the laser light illuminates the sample from the bottom side (iiib).

The sample is placed on a transparent glass plate with an anti-reflection coating (Glassplate, High AR coated 96–99% (400–700 nm)). The glass plate is mounted on a platform that is placed on an X–Y translation stage (v). The X–Y movement aligns the subject in respect to the camera axis. Depending on the desired resolution of each measurement the distance of the sample from the camera can be modified by placing the glass plate in one of the different fixed positions along the Z axis. The plate is mounted to the stages with a simple custom-made clip system so that it can be easily removed and put back in the setup for the repetition of the measurements. Images are captured by a thermoelectrically cooled 16bit CCD camera with a chip size of 1024 × 1024 pixels (Andor Corp., DV434, Belfast, Northern Ireland), which is mounted on the upper plate of the imaging box (vi). The CCD camera is equipped with a SIGMA 50 mm f/2.8 objective (Sigma Corporation, Tokyo, Japan) which was focused on the sample's surface. A filter wheel mounted in front of the CCD camera lens

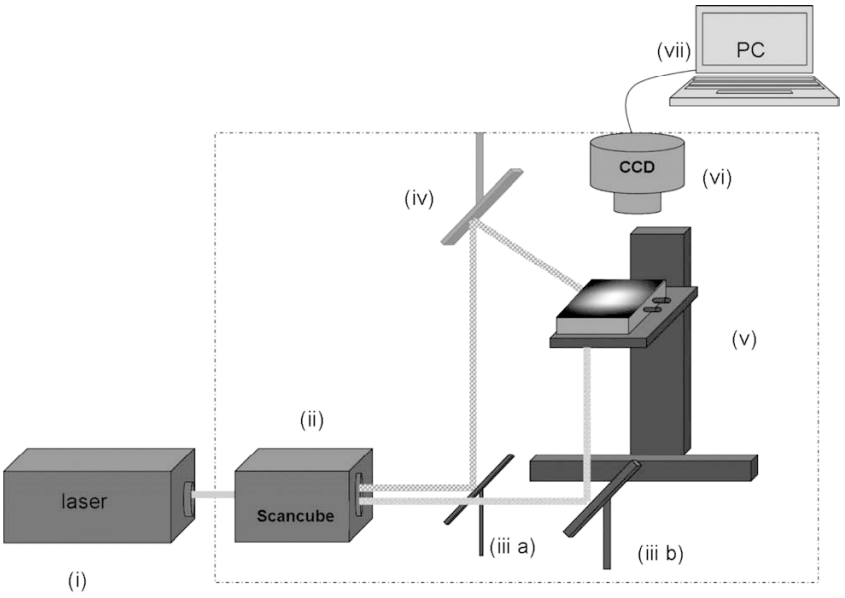

Fig. 1. A schematic representation of the experimental setup used for the tomographic acquisitions. The components of the system are shown as described in Sec. 2. On top of the sample, a raw image has been overlaid to illustrate the type of images obtained by the detector.

with different bandpass interference filters to enable the choice of the desired wavelength range of detection. We record the excitation images by using the 488 ± 30 nm and 510 ± 5 nm filters, respectively, in front of the camera and for the fluorescence images by using 540 ± 20 nm and 615 ± 45 nm filters, respectively, in front of the camera.

2.2. *FMT acquisition*

After placement of the sample on the imaging plate at the desired height, we choose the geometry of the measurements (transmission or reflection) and set the parameters of the experiment such as exposure time, excitation power, and number of illumination points (sources) according to size and shape of sample and resolution requirements of each experiment. Typical exposure times during the FMT acquisition for the excitation measurements was 0.1 s and for the fluorescence measurements 0.3 s.

2.3. *FMT reconstruction*

The data from the experiment are stored in the form of a stack of 2D images $I(x, y)$, which will be processed to obtain a 3D reconstruction of the fluorophore concentration inside the sample. Reconstruction of the fluorescence tomography data utilized normalized measurements where the fluorescence measurements are divided by the excitation light, accounting for any inhomogeneities of the sample affecting the propagation of light.[28] The fluorescence signal is expressed at a position r_d as:

$$U^{\text{fluo}}(r_s, r_d) = \frac{q^{\text{fluo}}}{4\pi D_{\text{fluo}}} \sum_{i=1}^{N} U^{\text{exc}}(r, r_s) N(r) \times G_{\text{fluo}}(r_d, r) \Delta V, \quad (1)$$

where q^{fluo} is a factor accounting for the detector quantum efficiency at the emission wavelength λ_b, the attenuation caused by the bandpass filter used in order to collect the emission light, D_{fluo} is the diffusion coefficient at the fluorescence wavelength, $N(r)$ is the fluorophore concentration and G_{fluo} is the Green's function solution to the diffusion equation and describes the propagation of the emission photon wave from the fluorophore to the detector in a slab configuration. Summation is performed over all source positions.

In an analogous way, the excitation intensity detected at the position r_d, is expressed as:

$$U^{\text{inc}}(r_s, r_d) \approx q^{\text{exc}} U^{\text{exc}}(r_s, r_d). \quad (2)$$

Equation (1) represents the first Born approximation,[29] q^{exc} is a factor accounting for the detector quantum efficiency at wavelength λ_α and the attenuation caused by the bandpass filter used in order to collect the excitation light.

Dividing Eq. (1) with Eq. (2) the expression for the normalized measurements is obtained[28]:

$$U^{nB}(r_s, r_d) = \frac{U^{\text{fluo}}(r_s, r_d)}{U^{\text{inc}}(r_s, r_d)} = \frac{1}{4\pi D_{\text{fluo}}} \frac{q^{\text{fluo}}}{q^{\text{exc}}} \frac{\sum_{i=1}^{N} U^{\text{exc}} N_t(r) G_{\text{fluo}} \Delta V}{U^{\text{exc}}(r_s, r_d)}. \quad (3)$$

In Eq. (3), U^{nB} is the measurement that, depending on the wavelength used for detection, we will from now on express as I_g or I_r, for the green and red filters, respectively. In terms of 2D data, since the detectors are located in a plane, U^{nB} can also be expressed as $U^{nB}(x, y; r_s)$, where we have separated the x and y components of the detector position. The expression shown in Eq. (3) is used in the final reconstruction after inverting with an Algebraic Reconstruction Technique (ART) with positive restriction[30] to create the map of the spatial distribution of the fluorophore concentration inside the reconstructed volume of our sample.

2.4. *Spectral unmixing*

Spectral unmixing methods exploit the fact that the detected fluorescence signal can be expressed as a linear combination of the different fluorescent components present in the sample, as long as the absorption at different wavelengths while traveling from the fluorophore to the detector is taken into account. If no spectral attenuation due to light propagation is taken into account, for each detection channel a linear equation can be derived that is comprised of the sum of the concentration of the fluorescence emitters multiplied by a weighting factor corresponding to the strength of the emission in that channel. Hence, if the number of detection channels is equal to the number of the investigated fluorescence targets a completely defined square system of equations can be derived and solved to calculate the unknown concentrations. In our study, two fluorophores were used: (a) Carboxyfluorescein succinimidyl ester (CFDA (5(6) — CFDA SE or CFSE) with an absorption peak at 492 nm and a fluorescence peak at 517 nm and (b) ATTO590 with a peak at 594 nm and a fluorescence peak at

624 nm and were used to simulate the emission of green and red fluorescent proteins. In this case, the fluorophore concentration reconstructions in each detection channel will correspond to the following linear equations:

$$\begin{aligned} I_g &= g_{\mathrm{CFSE}} C_{\mathrm{CFSE}} + g_{\mathrm{Atto590}} C_{\mathrm{Atto590}}, \\ I_r &= r_{\mathrm{CFSE}} C_{\mathrm{CFSE}} + r_{\mathrm{Atto590}} C_{\mathrm{Atto590}}, \end{aligned} \tag{4}$$

where I_g, I_r are the fluorescence reconstructions in the detection channels for CFSE and ATTO590, g_{CFSE}, g_{Atto590}, r_{CFSE}, and r_{Atto590} are the spectral strengths of CFSE and ATTO590. C_{CFSE} and C_{Atto} are the unknown reconstructed fluorophore concentrations of each fluorophore. If the previous system is expressed in matrix notation we obtain:

$$\begin{bmatrix} I_g \\ I_r \end{bmatrix} = \begin{bmatrix} g_{\mathrm{CFSE}} & g_{\mathrm{Atto590}} \\ r_{\mathrm{CFSE}} & r_{\mathrm{Atto590}} \end{bmatrix} \times \begin{bmatrix} C_{\mathrm{CFSE}} \\ C_{\mathrm{Atto590}} \end{bmatrix}. \tag{5}$$

The spectral strengths are calculated by integrating the signal under the part of the curve that corresponds to the spectral band allowed by each filter. Note that Eq. (5) does not take into account any spectral attenuation due to light propagation in a medium with spectrally dependent absorption. In this way if $g(\lambda)$ is the fluorescence spectrum of CFSE and $r(\lambda)$ the fluorescence spectrum of ATTO590, the spectral strengths could be defined as:

$$\begin{aligned} g_{\mathrm{CFSE}} &= \int_{520\,\mathrm{nm}}^{560\,\mathrm{nm}} g(\lambda) d\lambda, \\ g_{\mathrm{Atto590}} &= \int_{520\,\mathrm{nm}}^{560\,\mathrm{nm}} r(\lambda) d\lambda, \\ r_{\mathrm{CFSE}} &= \int_{570\,\mathrm{nm}}^{660\,\mathrm{nm}} g(\lambda) d\lambda, \\ r_{\mathrm{Atto590}} &= \int_{570\,\mathrm{nm}}^{660\,\mathrm{nm}} r(\lambda) d\lambda. \end{aligned} \tag{6}$$

In Eq. (6), the integration is performed on the width of the bandpass filter used for the corresponding detection channel. The solution of the system is given by the following equation that provides the unknown concentrations:

$$\begin{bmatrix} C_{\mathrm{CFSE}} \\ C_{\mathrm{Atto590}} \end{bmatrix} = \begin{bmatrix} g_{\mathrm{CFSE}} & g_{\mathrm{Atto590}} \\ r_{\mathrm{CFSE}} & r_{\mathrm{Atto590}} \end{bmatrix}^{-1} \times \begin{bmatrix} I_g \\ I_r \end{bmatrix}. \tag{7}$$

If the spectral attenuation of light propagation is to be accounted for, Eq. (7) needs to be applied directly to the reconstructed fluorophore concentration, taking into account the different wavelength dependence of the medium in Eqs. (1) and (3).

The values of the spectral strengths in Eq. (7) were calculated by measuring tubes with known concentration of each fluorophore in a commercial fluorimeter (FluoroMax-P, Horiba Jobin Yvon Inc., New Jersey, USA). Emission spectra were recorded by exciting the fluorophores at the same wavelengths used in the FMT. From the emission curves, the four spectral strengths are obtained by integrating at the appropriate detection area for both fluorophores. Figure 2 presents typical spectra of CFSE and ATTO590 obtained as described above as well as the spectral regions corresponding to the filters bandpass regions where the calculations of Eq. (6)

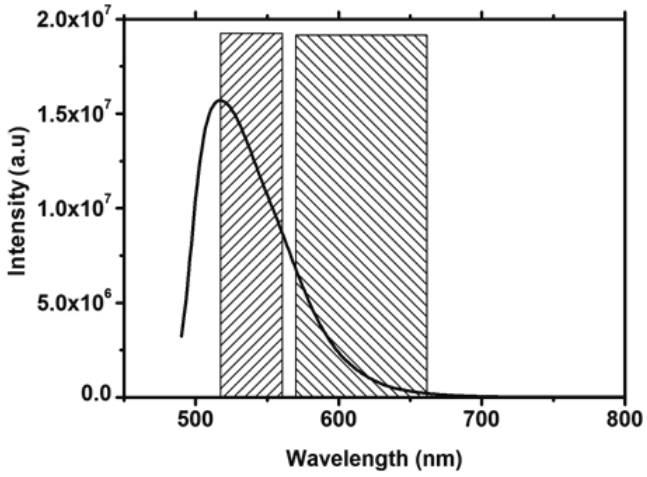

(a)

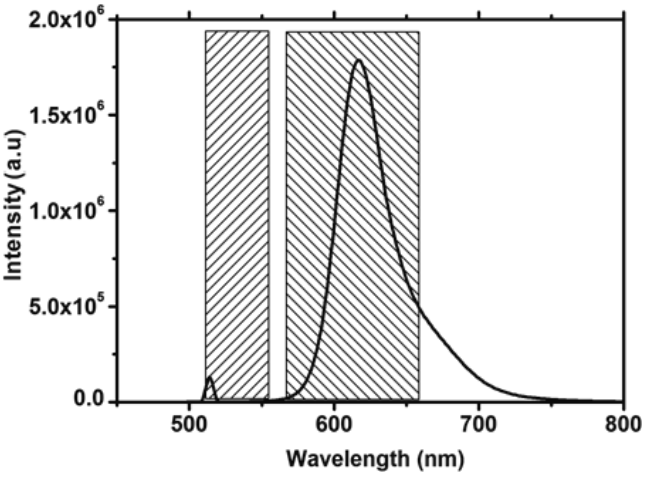

(b)

Fig. 2. The emission spectra of (a) CFSE and (b) ATTO590, obtained in a commercial fluorimeter as described in Sec. 2. The shaded areas correspond to the bandpass regions of the interference filters used to isolate the fluorescence signal. Integrating over these areas provides the spectral strengths used in the unmixing algorithm.

Table 1. Spectral strengths for CFSE and ATTO590.

g_{CFSE}	0.2058	r_{CFSE}	0.0761
g_{ATTO590}	0.000418	r_{ATTO590}	0.8798

are applied. The results of these calculations are shown in Table 1.

Once the FMT 3D reconstructions were obtained, arbitrary concentrations were converted to real concentration values by dividing the reconstructions with quantum yield, extinction coefficient, and path length for each excitation wavelength. These values were calculated from excitation spectra measured with the fluorimeter and by using the known values in a certain wavelength given by the manufacturer.

2.5. *Unmixing methods*

Two different unmixing methods were studied for the separation of the two fluorophores depending on the type of data it is applied to. The first method is applied on the raw 2D data while the second is applied on the reconstructed 3D data. The first is the common method used in microscopy and is also the method used up to date in tomographic approaches. Our goal is to study the efficiency, applicability, and accuracy of each method when applied to tomography where volumetric quantification is essential. In both cases, the spectral strengths were calculated as described above. In particular we consider the fact that, whenever wavelength-dependent attenuation is present, as in the case of blood or tissue, fluorescence intensity will be nonlinearly related to the optical properties of the tissue it traverses. Therefore, it is important to note that emitted light from each fluorophore will experience different attenuation depending on its wavelength, relative to its specific spectral overlap with absorbers found along its path length. This significantly hinders the use of multiwavelength unmixing on the raw 2D data when signals originate from inside the volume. In that case, if raw 2D data unmixing is performed, the quantified fluorophore concentration will be incorrect even if a qualitatively accurate 3D reconstruction is obtained.

2.5.1. *Unmixing the raw data (Unmix2D)*

In this method, the unmixing process is performed directly on the raw experimental data before the reconstruction. The algorithm described in Sec. 2.4 is applied on the raw recorded 2D images *pixel by pixel* and the unmixed raw data are then saved in an image stack which is used for the 3D reconstruction instead of the old data. This image stack is then processed with the FMT algorithms to produce the final reconstruction of the unknown (and now unmixed) fluorophore concentration.

2.5.2. *Unmixing the reconstructed data (Unmix3D)*

In this method the unmixing process of Sec. 2.4, in particular Eq. (7) is applied directly on the 3D reconstructed data. The reconstructions are performed separately for each detection channel providing two distinct reconstructed images for the green and the red detection channels which contain the contribution of both fluorophores inside the filter band. Then Eq. (7) is applied voxel by voxel to obtain the independent 3D distribution of the fluorophores' concentration.

2.6. *Phantom preparation*

The phantoms used in our experiments consisted of 20% Intralipid and black India ink both added to distilled water. The concentrations that we used were 5 ml Intralipid and 4.88 μl ink in a solution of 100 ml total volume, in order to achieve an absorption coefficient of approximately $\mu_a = 0.3\,\mathrm{cm}^{-1}$ and a reduced scattering coefficient of approximately $\mu_s' = 16\,\mathrm{cm}^{-1}$, both being realistic *in-vivo* values.[31,32] Fluorophores were added by using borosilicate microcapillary tubes (Drummond Scientific, US) with an outer diameter of 1.8 mm and an inner of 1.2 mm embedded inside the phantom at various depths.

As mentioned in Sec. 2.4, the two fluorophores that were used are (see Fig. 2): (a) CFSE for its similarities in absorption and emission characteristics to the Green Fluorescence Protein (GFP) and (b) ATTO590 for its similarities to the red fluorescent proteins.

The CFSE had a fixed concentration of 4 μM and the ATTO590 in three concentrations 5, 10, and 15 μM. The experiments were performed both in reflection and transmission geometry, using a 5×12 sources in an area of 100×250 mm. The height from the CCD camera was 15 cm, and the two tubes were placed in the sample at 7 mm distance and 3 mm below the surface.

The sample was illuminated by using two different wavelengths at 514 and 488 nm while fluorescence was recorded using two filters: a 40 nm bandwidth filter centered at 540 nm and a 90 nm bandwidth filter centered at 615 nm for green and red, respectively. The excitation signal of the laser was taken by a 10 nm bandwidth filter centered at 510 nm in the case of the 514 nm illumination, and with a 60 nm bandwidth filter centered at 480 nm for the case of the illumination at 488 nm.

3. Results

Our study aimed at assessing the best way of performing fluorescence unmixing in a tomographic problem. Spectral unmixing methods are very common in microscopy using 2D data, but as will be proven here in a tomographic approach handling 2D data may give incorrect results due to the attenuation of the fluorescent spectra as light travels through the highly scattering and absorbing medium. Here we have compared the

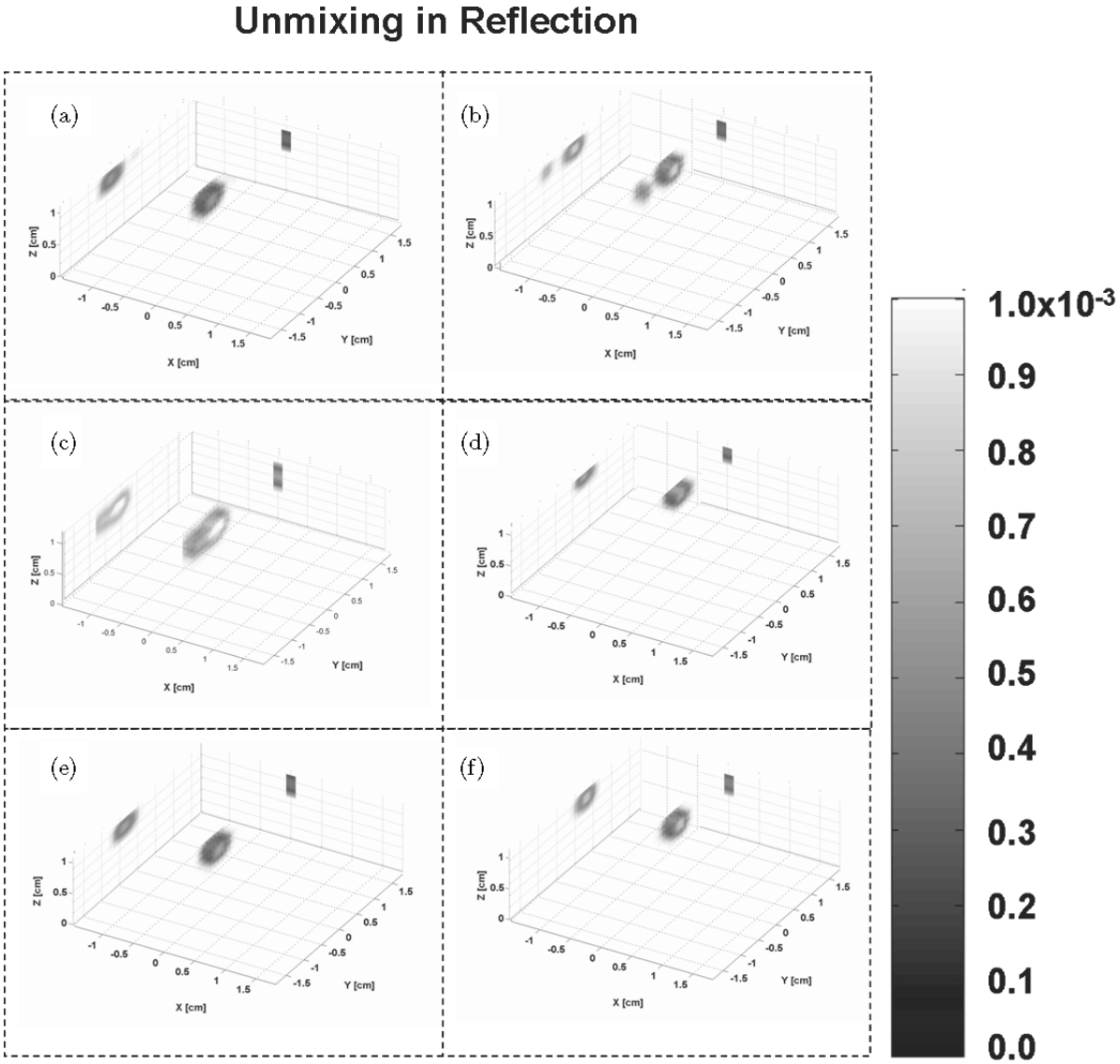

Fig. 3. 3D reconstructions of the two fluorophores in reflection geometry. (a) and (b) depict the unmixed reconstructions obtained in the two spectral regions for green and red channels, respectively. The projections of these reconstructions onto the xz and yz planes are also shown. (c) and (d) show the unmixed reconstructions for the green and red channels, respectively, for the case where the unmixing algorithm was applied to the 2D raw data. The projections of these reconstructions onto the xz and yz planes are also shown. Finally, (e) and (f) depict the unmixed reconstructions for the green and red channels, respectively, in the case where the unmixing algorithm is applied on the 3D reconstructed images. The projections of these reconstructions onto the xz and yz planes are also shown.

performance of our algorithm when applied to both 2D and 3D reconstructed data in both qualitative (unmixed reconstructions) and quantitative (retrieving the correct concentrations) terms, for both imaging geometries, namely reflection and transmission.

3.1. *Reflection geometry*

Figure 3 shows the results when using the fixed spectral strengths measured with a fluorimeter (described in Sec. 2.4) for the liquid phantom and for the first combination of concentrations ($4\,\mu$M CFSE and $5\,\mu$M ATTO590). Figures 3(a) and 3(b) present 3D images of the reconstructions for the green and the red channels, respectively, and are shown for comparative purposes. The projections of these reconstructions onto the xz and yz planes are also shown for better illustration. Reconstructions obtained after unmixing the 2D raw data are presented in Figs. 3(c) and 3(d) while in Figs. 3(e) and 3(f) the reconstructions correspond to unmixing the reconstructed 3D data obtained for each channel. The projections of the unmixed reconstructions onto the xz and yz planes are also illustrated and show that, in the case of unmixing the 2D raw data, fluorescence is reconstructed at the wrong depth and the location of the two tubes (CFSE and ATTO590), relative to each other, is incorrect. The reconstructions obtained after unmixing of 3D data instead correctly resolve depth and the relative position and size of the two tubes. From these figures it can be clearly inferred that in order to get the correct reconstruction and correct quantification the unmixing algorithm has to be applied to the volumetric data and not the 2D raw images.

Collective results can be seen in Fig. 4 where the concentrations retrieved from the FMT reconstructions are plotted against the real ones. The same region of interest was used in all calculations and the values obtained correspond to concentration units of μM. Figure 4(a) represents the results obtained after unmixing the raw data while Fig. 4(b) depicts the quantification results when unmixing the reconstructed data. Linear fits for the ATTO590 data were calculated for Unmix2D and Unmix3D with R^2 values of 0.9968 and 0.9996, respectively. It is clear that in the first case the obtained concentrations are not correct in terms of both absolute numbers as well as proportionality between CFSE and ATTO590.

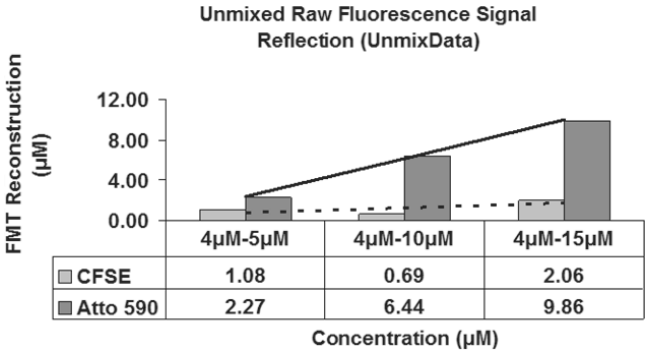

(a)

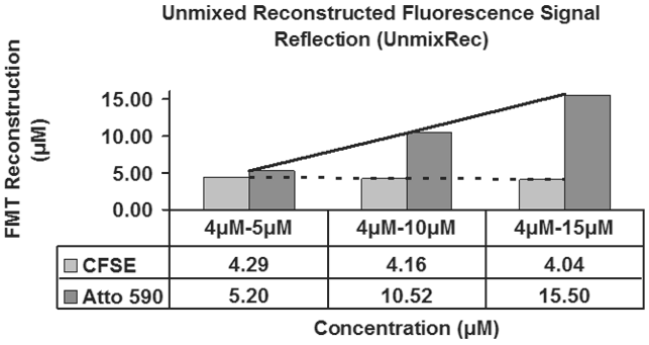

(b)

Fig. 4. Results of a quantification study with CFSE and ATTO590 performed in reflection and at different concentration pairs with only ATTO590's concentration being varied. The tables show the true concentrations and the ones obtained after unmixing. A linear fit has also been applied to the data for CFSE and ATTO590 to show the trend. (a) The obtained reconstructed concentrations in the case where the unmixing was applied to the raw data (the dotted and the solid lines represent linear fits to the data CFSE and ATTO590 data). (b) The obtained reconstructed concentrations in the case where the unmixing was applied to the reconstructed images (the dotted and the solid lines represent linear fits to the CFSE and ATTO590 data).

3.2. *Transmission geometry*

Similar results as in Sec. 3.1 were obtained in transmission geometry. Figures 5(a) and 5(b) present 3D images of the reconstructions from the green and the red channels, respectively, and are shown for comparative purposes. The projections of these reconstructions onto the xz and yz planes are also shown for better illustration. Similar to Fig. 3 for reflection geometry, Figs. 5(c) and 5(d) show the reconstructions after unmixing the 2D raw data while Figs. 5(e) and 5(f) represent the corresponding results for unmixing the 3D reconstructed data. The projections of these reconstructions onto the xz and yz planes are illustrated and confirm the results obtained in reflection geometry, with Unmix3D data

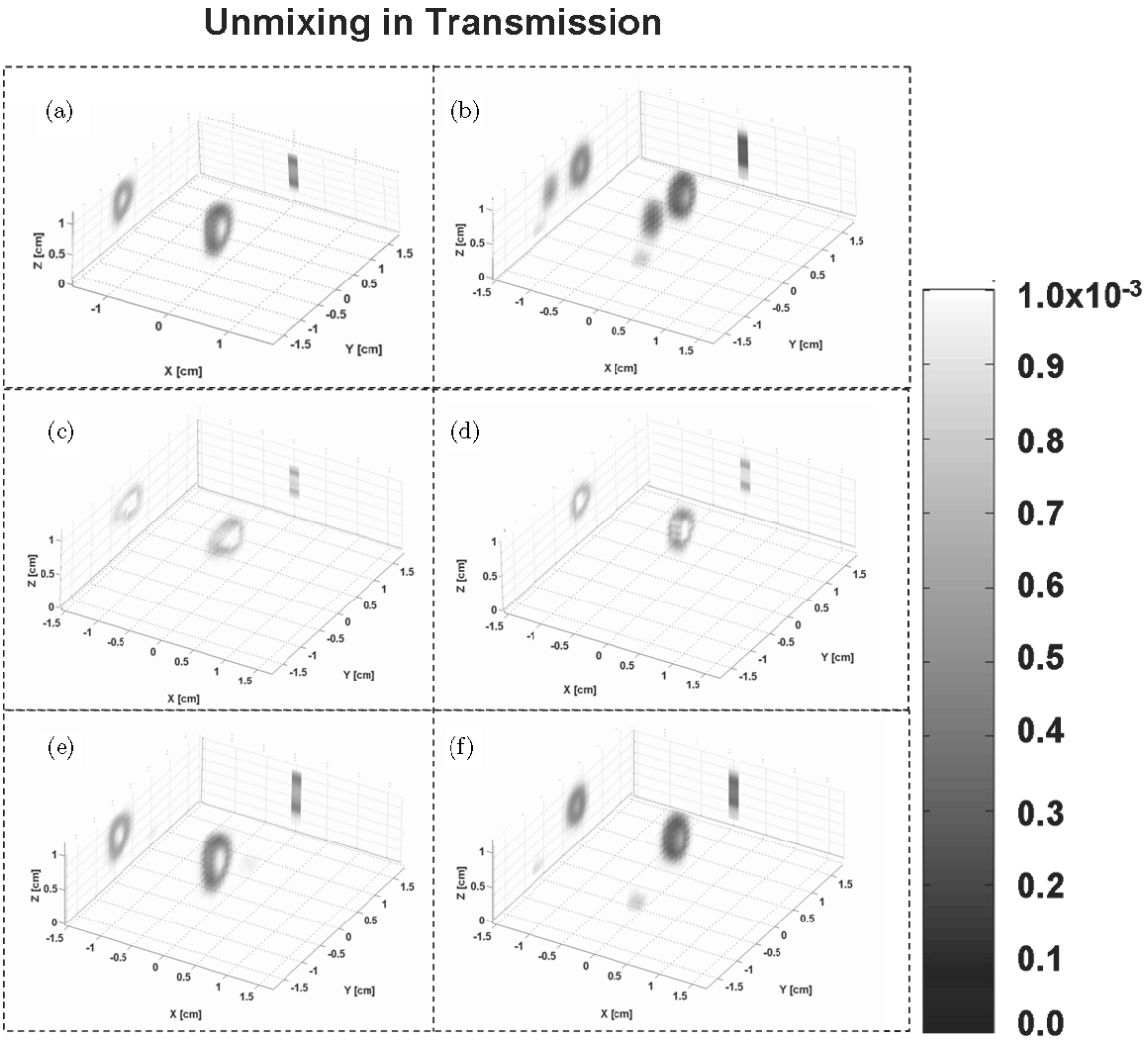

Fig. 5. 3D reconstructions of the two fluorophores in transmission geometry. (a) and (b) depict the unmixed reconstructions obtained in the two spectral regions for green and red channels, respectively. The projections of these reconstructions onto the xz and yz planes are also shown. (c) and (d) show the unmixed reconstructions for the green and red channels, respectively, for the case where the unmixing algorithm was applied to the 2D raw data. The projections of these reconstructions onto the xz and yz planes are also shown. Finally, (e) and (f) depict the unmixed reconstructions for the green and red channels, respectively, in the case where the unmixing algorithm is applied on the 3D reconstructed images. The projections of these reconstructions onto the xz and yz planes are also shown.

reconstructions providing better spatial resolution than Unmix2D data. Similar conclusions can be reached in transmission geometry: unmixing algorithms have to be applied volumetrically in order to have an accurate 3D reconstruction on the one hand and to retrieve correct concentrations on the other.

Collective results for the transmission geometry experiment can be seen in Fig. 6 where the concentrations retrieved from the reconstructions are plotted against the real ones. The same region of interest was used in all calculations and the values obtained correspond to concentration units of μM. Figure 6(a) represents the results obtained after unmixing the 2D raw data while Fig. 6(b) depicts the quantification results when unmixing the 3D reconstructed data. Linear fits have been applied to Unmix2D and Unmix3D data with R^2 values of 0.8453 and 0.9978, respectively. In the Unmix2D data, it is clear that obtained concentrations are incorrect in terms of both absolute numbers as well as proportions of CFSE and ATTO590. In contrast, the concentrations retrieved from the Unmix3D volumetric unmixing and shown in Fig. 6(b) are very close to genuine concentrations and the proportionality between CFSE and ATTO590 is correctly

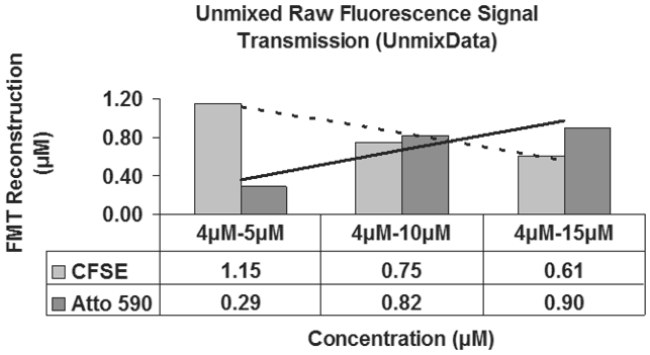

(a)

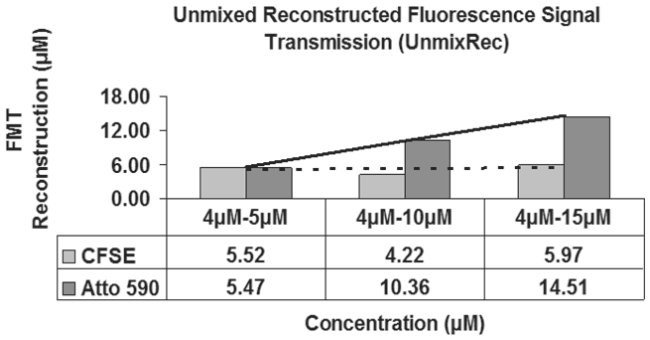

(b)

Fig. 6. Results of a quantification study with CFSE and ATTO590 performed in transmission and at varying concentration pairs with only ATTO590's concentration being varied. The tables show the true concentrations and the ones obtained after unmixing. A linear fit has also been applied to the data for CFSE and ATTO590 to show the trend. (a) The obtained reconstructed concentrations in the case where the unmixing was applied to the raw data (the dotted line represents a linear fit to the data). (b) The obtained reconstructed concentrations in the case where the unmixing was applied to the reconstructed images (the solid line represents a linear fit to the data).

recovered, concluding that the method of choice is to unmix the 3D reconstructed data.

4. Conclusions and Discussion

We have presented a tomographic unmixing method capable of separating different fluorophores with overlapping spectra. Our approach uses 3D reconstructed data rather than 2D raw measurements, as is common in microscopy and planar imaging. Comparing the experimental results when applying our algorithm to both raw and reconstructed data we have concluded that for accurate and quantitative tomographic imaging; unmixing has to be applied to the volumetric 3D data. When the 2D raw data are used, even in the cases where the reconstruction might appear correct, the retrieved concentrations are far from the true ones. However, when performing measurements in reflection geometry for superficial and small targets, such as subcutaneous lymph nodes, the 2D approach may give correct results since the light has only propagated for a few mean free paths inside the diffusive medium. This is important for *in-vivo* studies where the targets are subcutaneous and the 2D procedure allows for a much higher throughput. However, when deeper targets are considered the 3D approach is the only way of producing correct results, mainly due to the fact that the data have been treated with the appropriate model of light propagation before being unmixed and quantified.

A general comment with reflection geometry is that 3D reconstructions are underestimated on the z-axis, something that does not happen in transmission geometry. The reason for this behavior is that, in transmission, the volume of interest is much better probed in comparison to reflection geometry with the best solution being imaging from several angles to resolve sample depth. In conclusion, we have presented here a method capable of separating multicolor fluorescence signals in phantoms with accuracy in retrieving the correct concentrations $>96\%$ in transmission and $>88\%$ in reflection. Applications of the unmixing tomographic approach in realistic small animal biological models are manifold; distinguishing between several fluorescent proteins and/or dyes is in fact highly desirable and could provide a wealth of new information in many models including cancer, angiogenesis, gene regulation, and immune system studies, for example.

Acknowledgments

This research was supported by E.U. FP6 Integrated Project "Molecular Imaging" LSHG-CT-2003-503259 and E.U. FP7 Collaborative Project "FMT-XCT". R. F. acknowledges support from the Marie Curie Program EST-MolecImag Early Stage Training MEST-CT-2004-007643.

References

1. V. Ntziachristos, "Fluorescence molecular imaging," *Annu. Rev. Biomed. Eng.* **8**, 1–33 (2006).
2. V. Ntziachristos, C. Tung, C. Bremer, R. Weissleder, "Fluorescence-mediated molecular tomography resolves protease activity *in vivo*," *Nat. Med.* **8**, 757–760 (2002).

3. R. Weissleder, U. Mahmood, "Molecular imaging," *Radiology* **219**, 316–333 (2001).
4. G. Zacharakis, H. Kambara, H. Shih, J. Ripoll, J. Grimm, Y. Saeki, R. Weissleder, V. Ntziachristos, "Volumetric tomography of fluorescent proteins through small animals *in vivo*," *Proc. Natl. Acad. Sci. USA* **102**, 18252–18257 (2005).
5. X. Montet, J. L. Figueiredo, H. Alencar, V. Ntziachristos, U. Mahmood, R. Weissleder, "Tomographic fluorescence imaging of tumor vascular volume in mice," *Radiology* **242**, 751–758 (2007).
6. V. Ntziachristos, C. Bremer, R. Weissleder, "Fluorescence imaging with near-infrared light: New technological advances that enable *in vivo* molecular imaging," *Eur. Radiol.* **13**, 195–208 (2003).
7. V. Ntziachristos, J. Ripoll, L. Wang, R. Weissleder, "Looking and listening to light: The evolution of whole-body photonic imaging," *Nat. Biotechnol.* **23**, 313–320 (2005).
8. G. Zacharakis, J. Ripoll, R. Weissleder, V. Ntziachristos, "Fluorescent protein tomography scanner for small animal imaging," *IEEE Trans. Med. Imaging* **24**, 878–885 (2005).
9. V. Ntziachristos, C. Bremer, E. E. Graves, J. Ripoll, R. Weissleder, "*In vivo* tomographic imaging of near-infrared fluorescent probes," *Molecular Imaging* **1**, 82–88 (2002).
10. J. Ripoll, V. Ntziachristos, "Imaging scattering media from a distance: Theory and applications of non-contact optical tomography," *Mod. Phys. Lett. B* **18**, 1403–1431 (2004).
11. A. Garofalakis, G. Zacharakis, H. Meyer, E. N. Economou, C. Mamalaki, J. Papamatheakis, D. Kioussis, V. Ntziachristos, J. Ripoll, "Three-dimensional *in vivo* imaging of green fluorescent protein-expressing T cells in mice with noncontact fluorescence molecular tomography," *Mol. Imaging* **6**, 96–107 (2007).
12. V. Ntziachristos, B. Chance, "Probing physiology and molecular function using optical imaging: Applications to breast cancer," *Breast Cancer Res. Treat.* **3**, 41–46 (2001).
13. V. Ntziachristos, R. Weissleder, "CCD-based scanner for tomography of fluorescent near-infrared probes in turbid media," *Med. Phys.* **29**, 803–809 (2002).
14. E. E. Graves, J. Ripoll, R. Weissleder, V. Ntziachristos, "A submillimeter resolution fluorescence molecular imaging system for small animal imaging," *Med. Phys.* **30**, 901–911 (2003).
15. J. P. Culver, R. Choe, M. J. Holboke, L. Zubkov, T. Durduran, A. Slemp, V. Ntziachristos, B. Chance, A. G. Yodh, "Three-dimensional diffuse optical tomography in the parallel plane transmission geometry: Evaluation of a hybrid frequency domain/continuous wave clinical system for breast imaging," *Med. Phys.* **30**, 235–247 (2003).
16. R. B. Schultz, J. Ripoll, V. Ntziachristos, "Noncontact optical tomography of turbid media," *Opt. Lett.* **28**, 1701–1704 (2003).
17. S. R. Arridge, "Optical tomography in medical imaging," *Inverse Probl.* **15**, R41–R93 (1999).
18. B. W. Pogue, S. C. Davis, X. Song, B. A. Brooksby, H. Dehghani, K. D. Paulsen, "Image analysis methods for diffuse optical tomography," *J. Biomed. Opt.* **11**, 33001 (2006).
19. J. Ripoll, R. B. Schulz, V. Ntziachristos, "Free-space propagation of diffuse light: Theory and experiments," *Phys. Rev. Lett.* **10**, 103901-1–103901-4 (2003).
20. J. Ripoll, V. Ntziachristos, R. Carminati, M. Nieto-Vesperinas, "The Kirchhoff approximation for diffusive waves," *Phys. Rev. E* **64**, 051917 (2001).
21. T. Zimmermann, J. Rietdorf, R. Pepperkok, "Spectral imaging and its applications in live cell microscopy," *FEBS Lett.* **546**, 87–92 (2003).
22. G. Themelis, J. S. Yoo, V. Ntziachristos, "Multispectral imaging using multiple-bandpass filters," *Opt. Lett.* **33**, 1023–1025 (2008).
23. H. Tsurui, H. Nishimura, S. Hattori, S. Hirose, K. Okumura, T. Shirai, "Seven-color fluorescence imaging of tissue samples based on Fourier spectroscopy and singular value decomposition," *J. Histochem. Cytochem.* **48**, 653–662 (2000).
24. A. Papadakis, E. Stathopoulos, G. Delides, K. Berberides, G. Nikiforidis, C. Balas, "A novel spectral microscope system: Application in quantitative pathology," *IEEE Trans. Biomed. Eng.* **50**, 207–217 (2003).
25. T. Zimmermann, "Spectral imaging and linear unmixing in light microscopy," *Adv. Biochem. Eng. Biotechnol.* **95**, 245–265 (2005).
26. J. Swartling, J. Svensson, D. Bengtsson, K. Terike, S. Andersson-Engels, "Fluorescence spectra provide information on the depth of fluorescent lesions in tissue," *Appl. Opt.* **44**, 1934–1941 (2005).
27. A. D. Zacharopoulos, P. Svenmarker, J. Axelsson, M. Schweiger, S. R. Arridge, S. Andersson-Engels, "A matrix-free algorithm for multiple wavelength fluorescence tomography," *Opt. Express* **17**, 3025–3035 (2009).
28. V. Ntziachristos, R. Weissleder, "Experimental three-dimensional fluorescence reconstruction of diffuse media using a normalized Born approximation," *Opt. Lett.* **26**, 893–895 (2001).
29. M. Born, E. Wolf, *Principles of Optics: Electromagnetic Theory of Propagation, Interference and Diffraction of Light*, 6th edition, Cambridge University Press (1997).
30. C. Kak, M. Slaney, *Principles of Computerized Tomographic Imaging*, IEEE, New York (1988).

31. A. Torricelli, A. Pifferi, P. Taroni, E. Giambattistelli, R. Cubeddu, "*In vivo* optical characterization of human tissues from 610 to 1010 nm by time-resolved reflectance spectroscopy," *Phys. Med. Biol.* **46**, 2227–2237 (2001).

32. T. Durduran, R. Choe, J. P. Culver, L. Zubkov, M. J. Holboke, J. Gianmarco, B. Chance, A. G. Yodh, "Bulk optical properties of healthy female breast tissue," *Phys. Med. Biol.* **47**, 2847–2861 (2002).